DIRECT COMPARISONS OF HELICOPTER WAKE AND AIR LOADS FOR HOVER SIMULATIONS FROM THE AIAA HOVER PREDICTION WORKSHOP

Earl P.N. Duque, epd@ilight.com, Intelligent Light, United States
Atsushi Toyoda, at@ilight.com, Intelligent Light, United States
Michael D. Burklund, mdb@ilight.com Intelligent Light, United States
Nathan Hariharan, Nathan.Hariharan.ctr@hpc.mil, HPCMP CREATE-AV, United States
Christopher P. Stone, chris.stone@computational-science.com, Computational Science & Engineering, LLC, United States

ABSTRACT

Comparing many different CFD cases of the same problem is complicated by the use of differing meshes, solver codes, etc. The Helicopter Hover Prediction Workshop 2016 provides an opportunity to apply a standardized, automated post-processing workflow that eases dataset comparison, report generation and knowledge extraction for a diverse set of CFD results. This paper presents direct comparisons of the CFD simulation results submitted by the participants of the workshop. A standardized post-processing scheme based upon FieldView was developed that tracks the helicopter rotor tip vortex core for quantitative comparisons. Iso-surfaces and coordinate cut planes of Q-criterion were created and saved as FieldView XDB files for qualitative comparisons. These surface extracts allow interactive viewing and direct comparisons of the predicted wakes using multi window graphical displays. By comparing the rotor blade boundary surfaces against one consistent boundary surface, geometry differences were identified that may affect the comparisons. Proper comparisons require that all the datasets have similar normalizations. All appropriate normalizations were made to be consistent with PLOT3D normalization conventions. Several participants use wake filaments. These participants used FieldView particle file formats that enabled the creation of images and XDB's that directly compare the filaments between the various filament based solvers and the tip vortex paths predicted by the grid based solvers. In addition, standardized methods were developed that calculated sectional thrust and torque distributions that allowed for uniform comparisons across all datasets submitted. The paper herein presents submissions that utilized Reynolds-averaged Navier-Stokes solvers with overset, structured, unstructured, and hybrid Navier-Stokes/wake filaments.

1. INTRODUCTION

The helicopter community desires quality methods that allow for cost effective, accurate, and timely simulations of hovering flight. At SciTech 2014, the first invited hover prediction session was convened as motivated by the AIAA Applied Aerodynamics Technical Committee Rotorcraft Simulation Working group [1]. For the 2016 Hover Prediction Workshop, an open call resulted in twelve participants committing to submit work. This workshop requested that participants submit their results for three rotors based upon the S-76 rotor study by Balch and Lombardi [2] consisting of a swept tapered tip blade, a straight rectangular tip and a swept tapered tip with anhedral with a hover tip Mach number of 0.65 at sea level standard conditions.

In order to help standardize comparisons for the various types of datasets submitted and to maximize the knowledge extracted to improve hover prediction, a standard post-processing procedure was deemed necessary. It must be noted that the purpose of the resulting comparisons are not to determine which solution is better than another but rather to help gain the most understanding about the effects of the assumptions and resultant procedures used to perform hover predictions. Participants were encouraged to upload their grid and solution datasets to a centralized server for the three cases as shown in Table 1.

Table 1: Cases requested for comparisons

Case Hover tip Mach number = 0.65 at sea level standard conditions	**Identifier**
Swept Tapered Tip, $CT/\sigma = 0.09$	Case1
Straight, Rectangular Tip, $CT/\sigma = 0.09$	Case2
Swept Tapered Tip with Anhedral , $CT/\sigma = 0.09$	Case3

Seven participants submitted their solutions for case 1; their solution methodology is summarized in Table 2 and the baseline geometry shown in Figure 1. The size of the grids vary from over 200 million points and 5500 overset grids to as few as six grids and eight million grid points.

The cases submitted by Intelligent Light, (IL-F and IL-A) use the OVERFLOW2 solver[3]. For the IL-A case body grid adaption solutions were obtained for a total of five rotor rotations while the fixed grid case had no adaption and was ran for a total of 15 rotor revolutions. The Army case was performed by Jain [4] using the Helios code in unsteady RANS mode with 6169 overset grids totaling 286.3 million grid points. The Boeing [5] case is also an overset grid solution using the OVERFLOW2. Note that the Intelligent Light (IL-F and IL-A) case used the same near-body grids and solver inputs (e.g. turbulence model and dissipation terms) as the Boeing case. The main difference is that Boeing used cylindrical off body grids, and hence, the dominant flow direction is aligned with the tip vortex path. The Georgia Tech (GT) [6] case is a Hybrid/RANS code with structured grid near body solver based upon OVERFLOW2 and vortex elements for the wake. KAIST [7] uses an unstructured overset grid methodology with six grids totaling 23 million vertices and 33.8 million elements. ONERA [8] uses the elsA code, a block structured method with 53 grids totaling 10.8 million grid points. UTRC [9] represents a hybrid method with a structured-grid, Reynolds-averaged Navier-Stokes solver in the near-body and vortex elements for the wake.

Table 2: Dataset Identifiers, Grid Type and Solver Formulations

Identifier	Organization	Grid	Formulations	Grid Specs
IL-F	Intelligent Light	Structured Overset Fixed Cartesian	URANS OVERFLOW2 Same Inputs as Boeing	Grids=119 Points=226,756,734 Revs=20
IL-A	Intelligent Light	Structured Overset Adaptive	URANS OVERFLOW2 Same Inputs as Boeing	Grids=5502 Points=214,960,101 Revs=5
Army	Army-ADD, Moffett Field	Structured Overset Adaptive	URANS HelOS	Grids=6169 Points=286,307,735 Revs=unknown
Boeing	Boeing	Structured OVERSET	URANS OVERFLOW2	Grids=17 Points=63,407,653 Revs=20
GT	Georgia Tech	Structured	RANS/Hybrid	Grid - ¼ Domain
KAIST	KAIST	Unstructured Overset	URANS	Grids=6 Nodes=23,070,265 Elements=33,840,742 Revs= unknown
ONERA	ONERA	Structured	RANS	¼ Domain Grids=53 Points=10,690,947
UTRC	UTRC	Structured	RANS/Hybrid	Grids=436 Points=8,399,220 Revs=20

Table 3: Dataset Set Size and Reduction

Identifier	Organization	Grid and Q	XDB
IL-F	Intelligent Light	Grid – 6G Soln- 12G	1.548G
IL-A	Intelligent Light	Grid – 5.1G Soln- 11G	3.16G
Army	Army-ADD, Moffett Field	Grid – 5.5G Soln- 6.9G	1.61G
Boeing	Boeing	Grid – 1.7G Soln- 6.7G	0.975G
GT	Georgia Tech	Grid – 1.3G Soln- 1.7G	0.013G
KAIST	KAIST	Grid/Soln – 3G	0.637G
ONERA	ONERA	Grid – 0.286G Soln- 0.408G	0.153G
UTRC	UTRC	Grid – 0.585G Soln- 0.975G	0.136G

This paper presents the methodologies that were used to visualize and quantitatively compare the contributed participant datasets listed in Table 2. Results of these visualizations are then presented for discussion by all the participants of the workshop.

2. DATASET COMPARISONS

The data comparisons presented in this paper relied upon a FieldView XDB workflow. Figure 2 illustrates a typical file-based, volumetric data post-processing workflow. In this workflow, the solver writes files to disk of the complete grid and solution volume. The post-processor then reads the volume data and computes the various graphics based objects such as geometric surfaces, coordinate cutting plans, iso-surfaces of arbitrary scalar functions, streamlines, etc.. After the post-processing objects are created, they are then further processed to render a graphical image, integrate functions on surfaces to yield integral quantities like force and moments, and plot values on the surface such as the pressure coefficient (Cp) distributions.

Much of the computational costs and wall-clock time is taken up by the post-processing tool reading the volume dataset and creating the post-processing objects. In a typical workflow, the post-processing objects are thrown away at the end of the session. As shown in Figure 3, in a FieldView XDB workflow, the post-processing objects are saved as XDB files that can be used for future, repeated use.

Furthermore, the XDB file can be created by executing FieldView in batch on a large HPC system or they can be created interactively and saved. In either method, the XDB file can then be read into FieldView where all other post-processing actions can be performed on the XDB extracts. Since the extracts are at the fidelity of the original data, there is no loss in accuracy yet several orders of magnitude of data reduction can be obtained.

Using a FieldView XDB workflow, the volume datasets submitted by the participants were reduced to sets of coordinate surfaces, boundary surfaces, and iso-surfaces as illustrated in Figure 4. These extract types were designed to enable direct comparisons between datasets. FieldView's FVX programming language was used to automatically create the surfaces in batch and export them to files as FieldView XDB datasets. These data files will be made available to all the participants for download and their own use. To explore these data extracts, participants will be able to use their own licensed version of FieldView or download the free viewer, XDBView, from the Intelligent Light website.[*].

FVX scripts were created to automatically generate images, tables, and 2-D plots using gnuplot. Specialized procedures were developed to detect and track the tip vortex core and then generate comparison plots to quantitatively compare the first blade passage and miss distance. Iso-surfaces of Q-criterion and coordinate cut plane in azimuth angle and z-axis were created and exported as XDBs. These XDB's were then used to create images that compare across participant submissions using multi window plots and difference plots. Azimuth cut-planes (theta) were created every 5 degrees from 0 – 360 degrees. Z-axis coordinate cut-planes were also created at every inch from 10 inches below to 10 inches above the rotor center, which allowed for induced velocity profiles comparison.

In order to provide consistent comparison among datasets, all datasets were normalized to be consistent with OVERFLOW/PLOT3D normalizations where by the reference freestream velocity is the speed of sound (a_{inf}). Temperature and density were normalized by the freestream values. The grid scale is in inches.

The Q-criterion was exported to the coordinate cut surfaces and used to identify the tip vortex core centers. To track the vortex core geometric center, the approximate initial center location was seeded manually at 5 degrees behind the reference blade. This first seed was placed well away from the blade trailing edge to avoid the noise of Q-criterion values found near the blade boundary surface. To isolate the vortex cores, the Q-criterion on the first azimuth plane (5^o behind the blade) is used along with a threshold function with values of Q-criterion set between 0.001 to the maximum Q-criterion value. This setting results in a region of grid points that surround the vortex core. The average of all remaining points on the thresholded surface are then used to define the geometric center of the vortex core. The process is repeated by looping through each azimuthal cut-plane every 5 degrees. The search continues until there are no points found within the given search region and the vortex core geometric center cannot be determined. The vortex core center positions and estimated core diameter are then written to a table. In addition, a separate file in FieldView's FVP (particle path file) format is written out. The FVP file was used by FieldView along with the iso-surface XDB of Q-criterion to visualize the tracking of the vortex core center. The table data of the vortex core centers were also used to create 2D plots using gnuplot for comparison plots among the participants. Finally, for hybrid methods, the vortex wake data were written to FieldView FVP files that were subsequently used to enable imaging filament calculations for direct comparisons.

The rotor blade geometry may have a significant effect upon the hover predictions. Rendering images of each user's blade boundary surface against the Intelligent Light (IL-F and IL-A) allowed for quick comparison on the differences between the blade surfaces.

Finally, standard FVX scripts were created that performed sectional load calculations. To enable this capability, the local Cp was calculated on the rotor blade boundary surface using the standard PLOT3D normalizations as shown in (1). A radial threshold function was applied to form a thin radial slice of width Δr. The local Cp was integrated upon the slice with the appropriate unit normal to arrive at the thrust the torque, (2) and (3), respectively. The threshold was then advanced to the next radial slice and the integration was repeated until the entire span was integrated. Since each participant data used different normalization, a formula function file was used to convert all the cases to the same normalized unit

[*] Download XDBView from:
http://www.ilight.com/en/products/xdbview-2

system. Note that the thrust and torque coefficients presented here only consider the pressure component and ignore the viscous contribution.

$$\boldsymbol{C_p} = \frac{\left(\boldsymbol{P}-\frac{1}{\gamma}\right)}{\frac{1}{2}\left(\frac{r}{R}\boldsymbol{M_{tip}}\right)^2} \tag{1}$$

$$c_t = \frac{r \oiint \; C_p\, n_z\, dA}{R\, \Delta r \cdot chord} \tag{2}$$

$$c_q = \frac{\oiint \; C_p\, n_x\, dA}{\Delta r \cdot chord} \tag{3}$$

Where:

$C_p =$ local pressure coefficient, c_t = local thrust coefficient, $c_q =$ local torque coefficient, $p =$ non-dimensional pressure, $\gamma =$ gas constant (1.4),),), $dA =$ surface area integrand in grid units, $\Delta r =$ integration surface width in grid units, $r =$ radius to center of integration surface in grid units, $R =$ blade tip radius in grid units, $chord =$ blade chord at center of integration surface in grid units, $n_x =$ unit normal in x-direction, $n_z =$ unit normal in z-direction, $M_{tip} =$ hover tip Mach number

3. RESULTS

The comparisons start with the grids used by IL-F [3], Army [4], Boeing [5] and KAIST [7]. Figure 5 provides orthonormal views of the coordinate grid cuts at azimuth angle of 0^o. IL-F shows the uniform grid in the off-body Cartesian grids designed to capture the wake. The Army method uses overset, body-fitted, near-body structured grids with Cartesian adaptive off-body grids. KAIST uses an overset grid with a near-body unstructured grid surrounded by Cartesian grids off-body. The grid refines as it approaches the blade tip. Boeing uses a cylindrical grid and manually clusters the grid vertically along the z-axis around the blade region and radially in the area of the wake contraction.

The definition of the blade surface may have significant effects upon the hover prediction. Figure 6 and Figure 7 provide comparisons between the Intelligent Light (IL-F and IL-A) blade boundary surface and Georgia Tech (GT) and UTRC; Boeing and the Intelligent Light (IL-F and IL-A) use the exact same near body grids. As shown in Figure 6, the Georgia Tech (GT) surface has a higher collective angle as evidenced by the red Georgia Tech (GT) blade boundary surface protruding along the top leading edge just ahead of the ¼ chord line and along the bottom surface aft of the ¼ chord line. The UTRC blade boundary surface has similar differences indicating a possible collective angle difference. However, there may also be a twist difference since the differences along the bottom surface do not follow the ¼ chord line like the Boeing boundary surface. There also appears to be a significant difference just outboard of the knee of the sweep section. Note that these surface differences just state that the surface is different from the Intelligent Light (IL-F and IL-A) and Boeing and does not judge which geometry is the true geometry. These differences should be considered when evaluating the following visualizations and plots.

Figure 8 shows the comparisons of the z-velocity along the coordinate cut planes at x = 0.0 (theta = 0^o). The Georgia Tech solution does not show a coordinate cut surface because it is a hybrid case and the blade is a near body grid only very close to the blade surface. The UTRC case is also a hybrid method but with the grid extending further out than Georgia Tech.

All users show wake contraction while IL-F, Army, Boeing, and KAIST tend to show some mixing/perturbations of the wake downstream beginning around ¾ of a center body length. The IL-A case has not fully developed. It has been run only five rotor revolutions. The initial starting vortex in the wake persists as evidenced by the dark regions extending radially beyond the wake contraction region along the bottom of the image. The ONERA and UTRC cases show very smooth wake contraction downstream of the rotor.

Figure 9 shows a comparison of the inflow velocities along a plane just above the rotor blade tip path plane. A radial threshold removed any grid points greater than a radius of 75 inches (roughly 20 inches beyond the blade tip). The inflows look very similar. However, Boeing has noticeable asymmetry around the center body. Intelligent Light (IL-F and IL-A) is also asymmetric around the center body with some up welling of small flow structures. The flow asymmetry may be artifacts of unsteady flow and three-dimensionality that may be lost when the flow field is averaged across 1 or more rotor revolutions or when symmetric boundary conditions are assumed. The ONERA case uses a period condition to model the 4 rotors; hence only ¼ azimuth is shown. The UTRC case, a hybrid case, only grids a small region surrounding the rotor blade. The inflow pattern for UTRC looks similar to the others, but the volume data only contains one blade-lifting surface and the surrounding section.

Figure 10 and Figure 11 compare the iso-surface of Q-criterion. In all cases the surfaces were defined by Q-criterion=0.001 and then colored by z-velocity. All cases show the tip vortex forming and coiling up into its characteristic helix pattern for several blade passages.

The IL-A and the Army approach utilize an offbody adaptive scheme which captured fine details of the wake. The IL-A solution clearly shows several passages of the blade tip vortex. Interestingly the adaptive solutions are also characterized by vortex instabilities and secondary vertical flow patterns (“vertical fingers” or “worms”) which are not present in other solutions. The Boeing approach with a system of fixed cylindrical grids to capture the wake does a reasonable job of capturing several vortex passages, but the vortex is lost as the grid stretches beneath the rotor. Likewise is true for the KAIST solutions, which uses a system of fixed grids in the wake. Secondary vortex flow structures seen in the adapted grid approaches may be due to the captured vortex strength or multiple block-to-block communication that naturally occurs in grid-adapted solutions.

The ONERA case forms a tip vortex but at this Q-criterion value it dissipates after 1 blade passage. Here are also artifacts at grid boundaries that may be numerical artifacts from either the solver, from post-processing errors due to gradient discontinuities at grid boundaries, or a combination of both.

Figure 12 present isometric views of the vortex wake tracking paths overlayed with iso-surfaces of Q-criteria for both the grid based solutions (IL-A, IL-F, Army, Boeing, KAIST and ONERA) as determined by the Q-criterion based tracking procedure and the vortex paths determined directly by the hybrid solvers (Georgia Tech and UTRC) solvers. The behavior of the wake tracker applied to Boeing is characteristic of the grid-based methods. The wake centers descend and smoothly contract radially as expected, and then they begin to fluctuate. The wake center paths eventually begin to wrap around each other and then the tip vortex either dissipates or breaks up. For the hybrid methods, the wake follows a smooth path for a large number of rotor rotations; the figure does not show the entire wake path.

Figure 13 - Figure 15 give a closer qualitative comparison of the vortex core path from the tip, its contraction, and the blade miss distance at the first blade passage. As shown in Figure 13, the vortex core for the four grid based methods (IL-F, Army-Boeing and KAIST) start 5 degrees behind the rotor by design; the coordinate cuts are every 5 degrees thereafter. The cores exhibit some variation. The two hybrid methods start at different locations. One item of note is that the Georgia Tech case, there are several vortex paths that were provided and one was arbitrarily selected for presentation.

The wake contraction illustrated in Figure 14 shows the rotor blade system with the reference blade 1 located at the 12 o'clock position. The image shows very similar contraction for the first blade passage after 90^0 clock-wise from blade 1. After the 2^{nd} blade passage the contraction trends begin to move apart and by the 3^{rd} blade passage there is some considerable spread. By the 4^{th} passage, we see the grid based methods starting to break up, exhibit vortex pairing or completely disappear. For the hybrid cases, the vortex persists as expected.

Figure 15 provides a qualitative view of the vortex core first blade passage miss-distance. As shown, all but one (Georgia Tech) exhibit a similar miss distance. Note again that the Georgia Tech solution was arbitrarily selected and other vortex paths in that dataset may have different behavior.

Figure 16 completes the comparison of the wake vortex centers by plotting the wake contraction (R) vs wake descent (Z). The figure shows that initially the wakes descend and contract similarly and then large differences begin to form. In particular, Georgia Tech (GT)'s wake center tends to flatten out then descend again. At around Z=9 inches, all methods show that the wake begins to meander and no longer follow a theoretical wake descent and contraction.

Finally, for C_T=0.09 solutions provided by the participants, the local torque and thrust coefficient comparison in Figure 17 show some considerable similarities and differences for the various methods. For the torque, the trend for all have similar behavior across blade span. For 40%< r/R < 90% blade span, the torque is relatively flat varying between 0.03 and 0.045 with a sharp increase and decrease behavior at r/R > 90%.

For the local thrust coefficient, IL falls outside of the trend shown by the other methods. For r/R > 30%, Boeing, Army, Georgia Tech, ONERA and UTRC have very similar thrust trends. However for r/R<30%, UTRC and Georgia Tech diverge from ONERA, Army and Boeing. For r/R > 70%, IL-A and IL-F begin to follow the trend of the other methodologies and above 90% all the methods have similar traits.

4. CONCLUSION

Detailed direct comparison of 3D computed hover flowfields form the 2016 AIAA hover prediction workshop was conducted. All the participants uploaded the full 3D computed flowfield for a specified trimmed thrust hover case. A FieldView XDB workflow was created to process all of the datasets (structured, unstructured, and hybrid) and extract visualizations and plots of key physics such as tip-vortex wake, wake trajectory, inflow patterns, surface Cp's, etc. This is perhaps a first-of-its-kind effort for any aerospace technical workshop.

A subset of the data compared has been presented in this paper. Both qualitative and quantitative comparisons of the blade geometries and of the vortex wake were performed. Some differences in the blade collective and possibly blade twist were found in the participant submissions. The wake comparisons showed similar behavior for the first blade passage but then as the wakes descend they tend to have very different behavior. The ability to capture the unsteadiness in the wake and the three-dimensionality resulted in asymmetric flow behaviors that could be lost if averaging and symmetry boundary conditions were used.

5. ACKNOWLEDGMENTS

The authors would like to thank Cray Inc. for providing access to the corporate Cray XE6 computer, Kaibab, where the Intelligent Light (IL-F and IL-A) OVERFLOW2 solutions were performed. We also would like to thank R Systems NA, Inc. for providing their High Performance Computer Cluster systems that were used as a common data repository for the participants and for data post-processing. Final thanks to Mr. Steve Legensky, General Manager, and Founder of Intelligent Light for supporting our participation in this project as part of our persistent drive to advance CFD post-processing

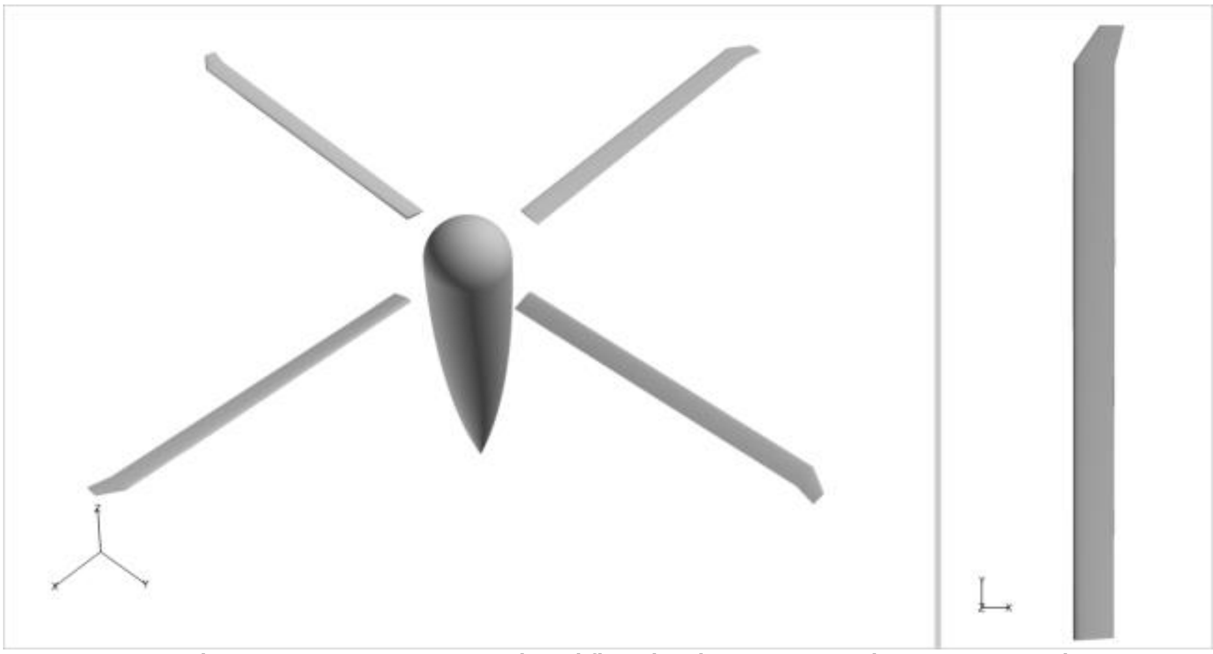

Figure 1: Geometry - Focused workflow development upon the swept-tapered

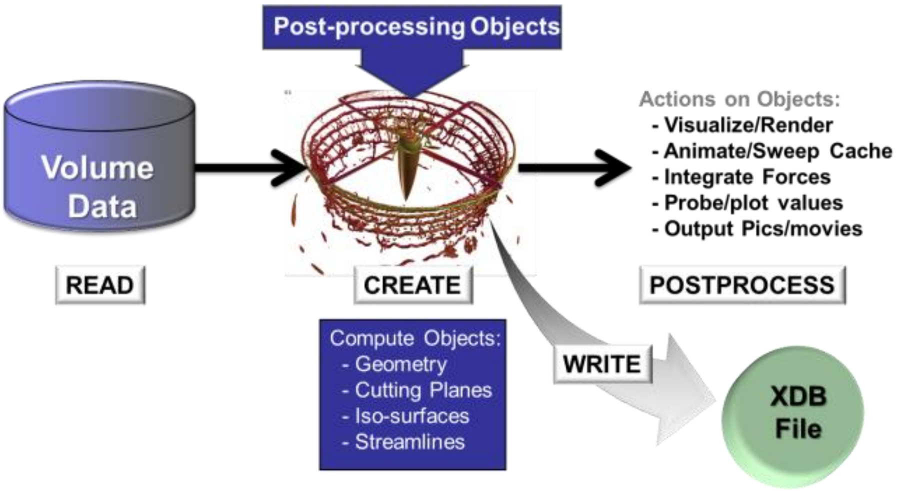

Figure 2: Volume Data Processing

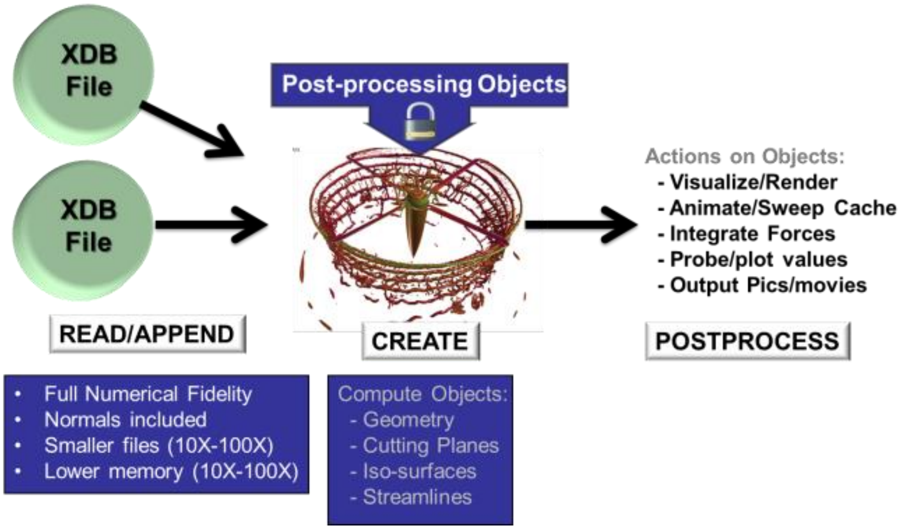

Figure 3: FieldView XDB Schematic

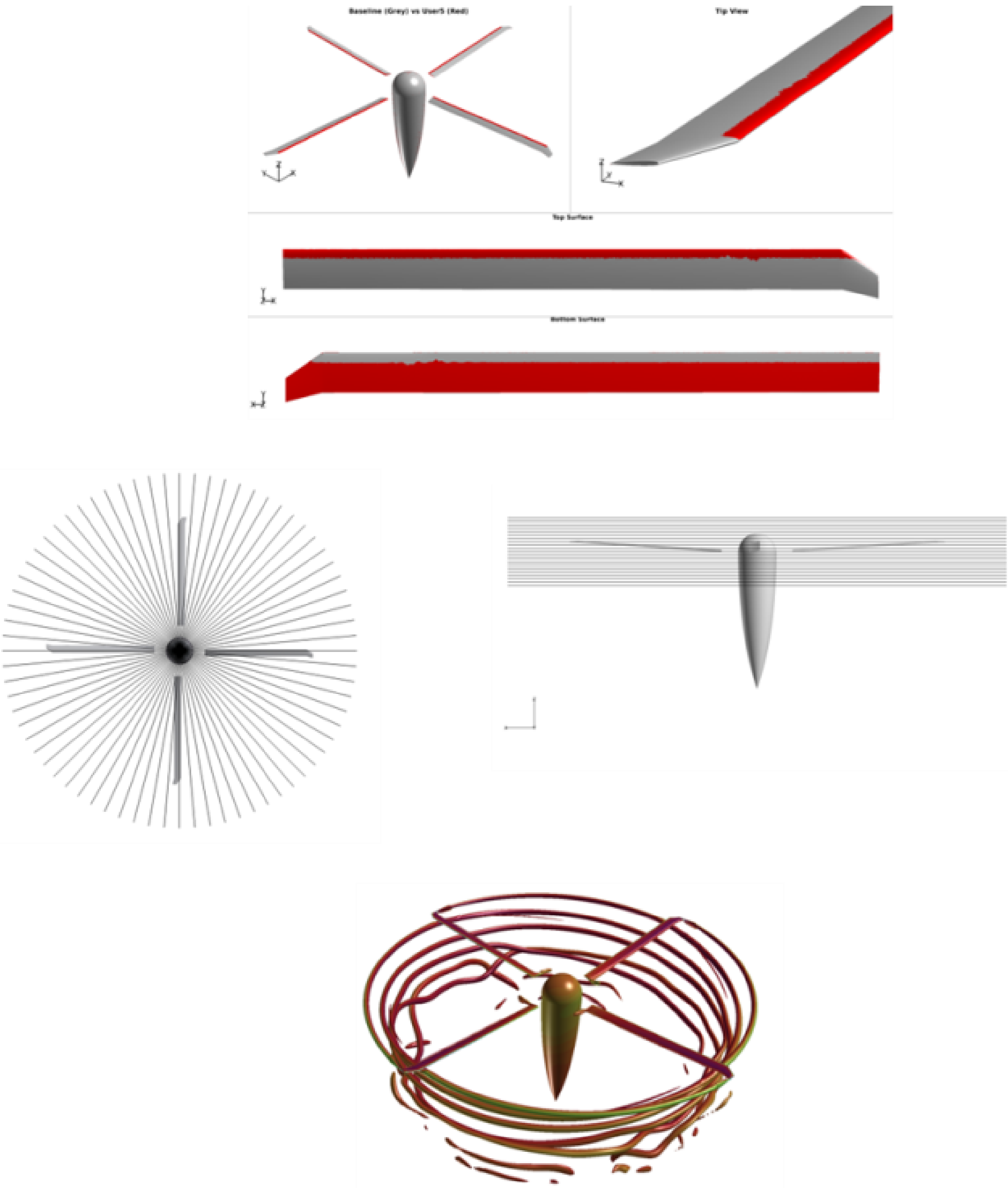

Figure 4: Extract Types

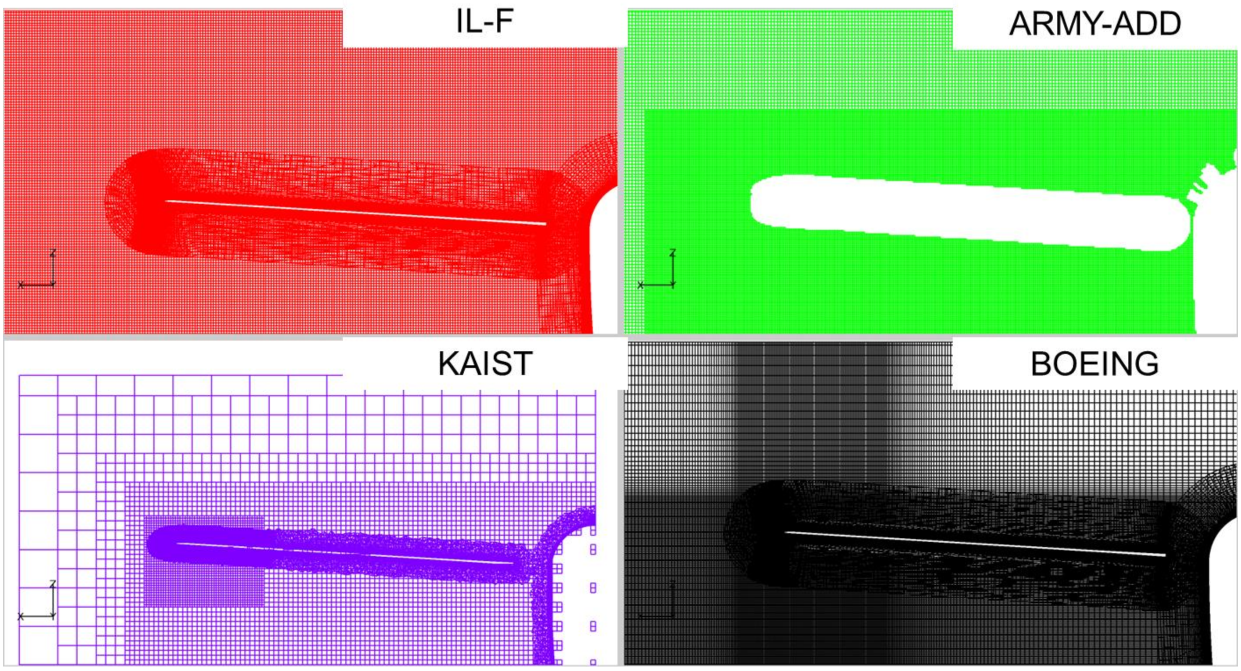

Figure 5: Grid Resolution Comparison

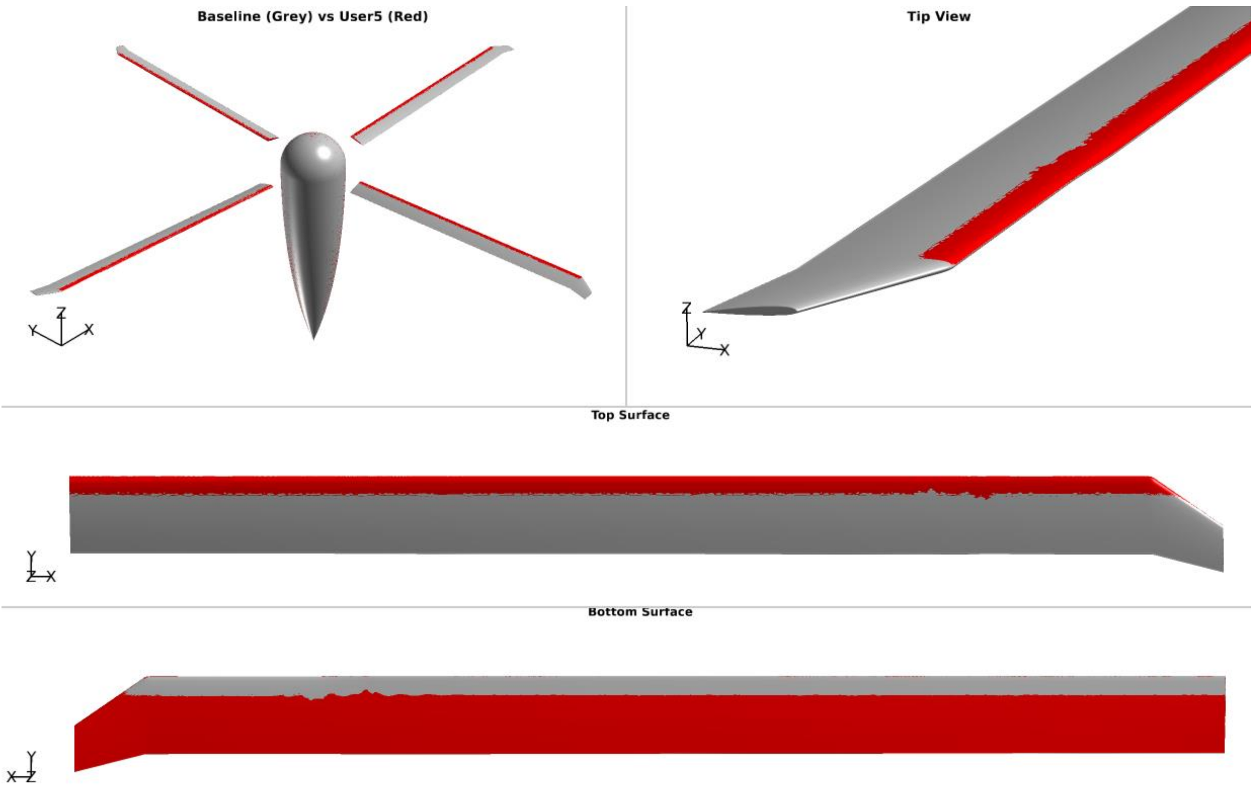

Figure 6: Comparison Intelligent Light (IL-F and IL-A) (Grey) vs Georgia Tech (GT) (Red)

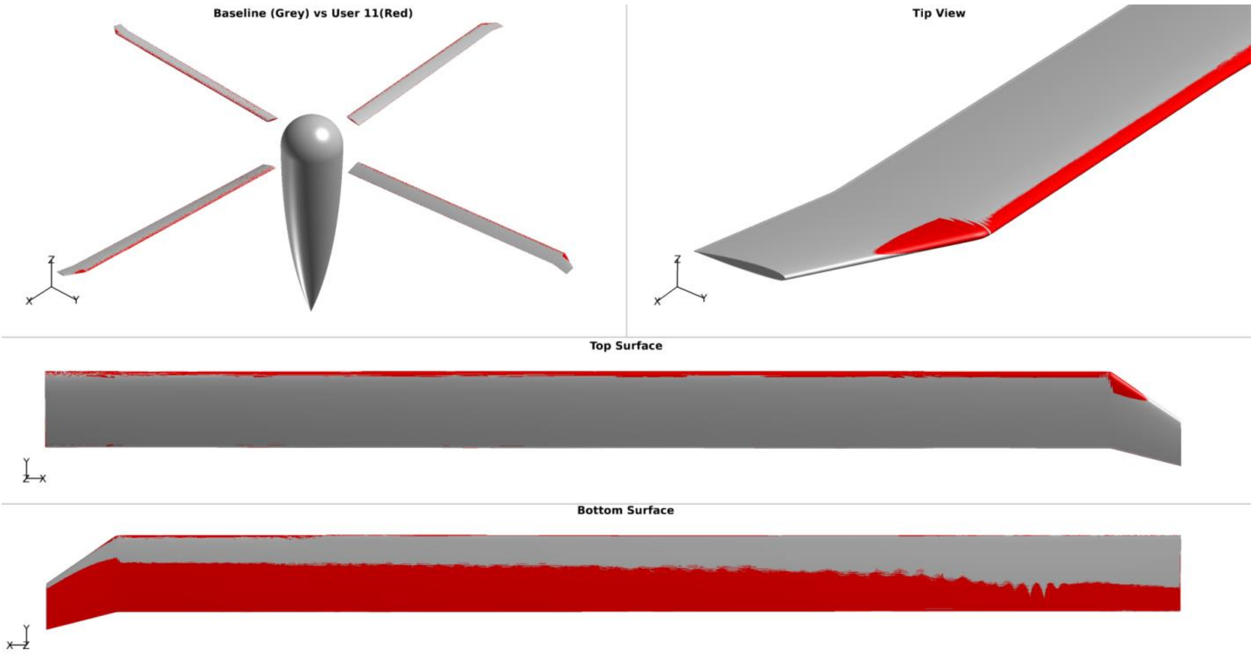

Figure 7: Comparison Intelligent Light (IL-F and IL-A) (Grey) vs UTRC (Red)

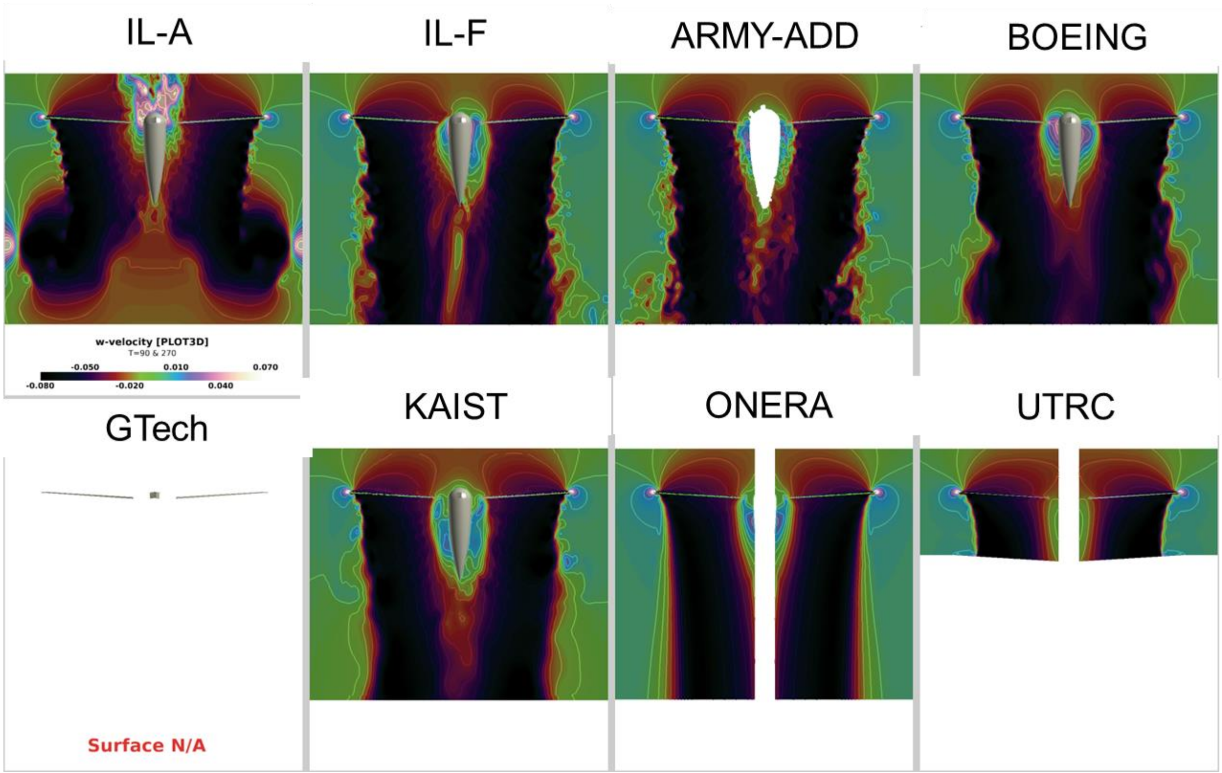

Figure 8: Comparison of w-velocity @ Coordinate Cut Plane X=0.0

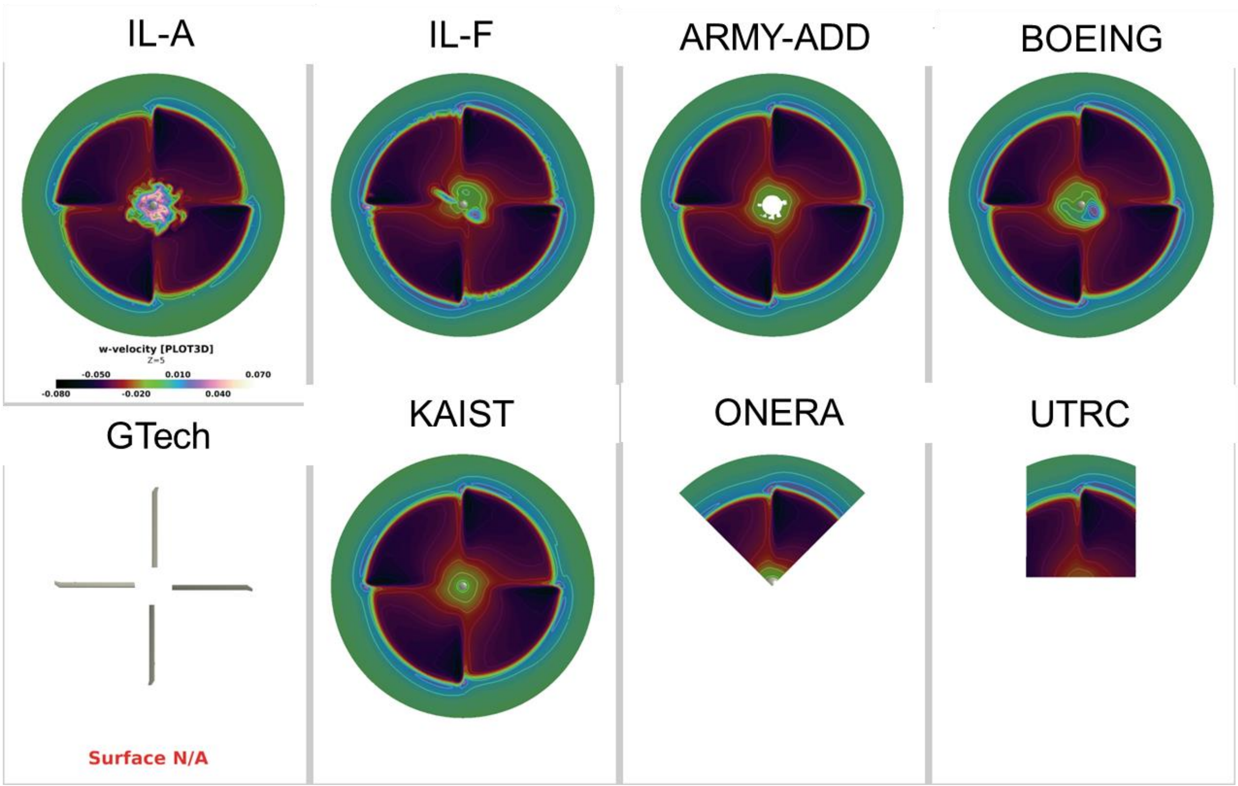

Figure 9: Comparison of w-velocity @ Coordinate Cut Plane Z=5.0

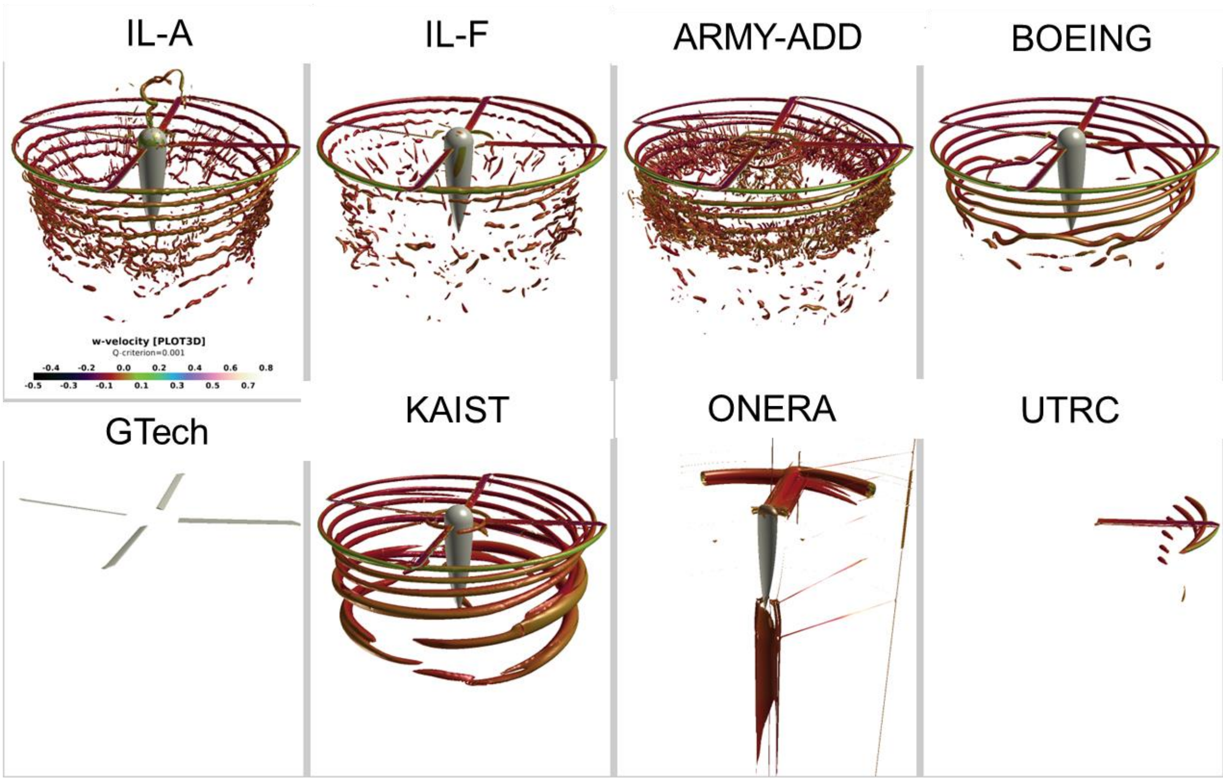

Figure 10: Iso View Comparison of Iso-surfaces of Q-Criterion =0.001 colored by w-velocity

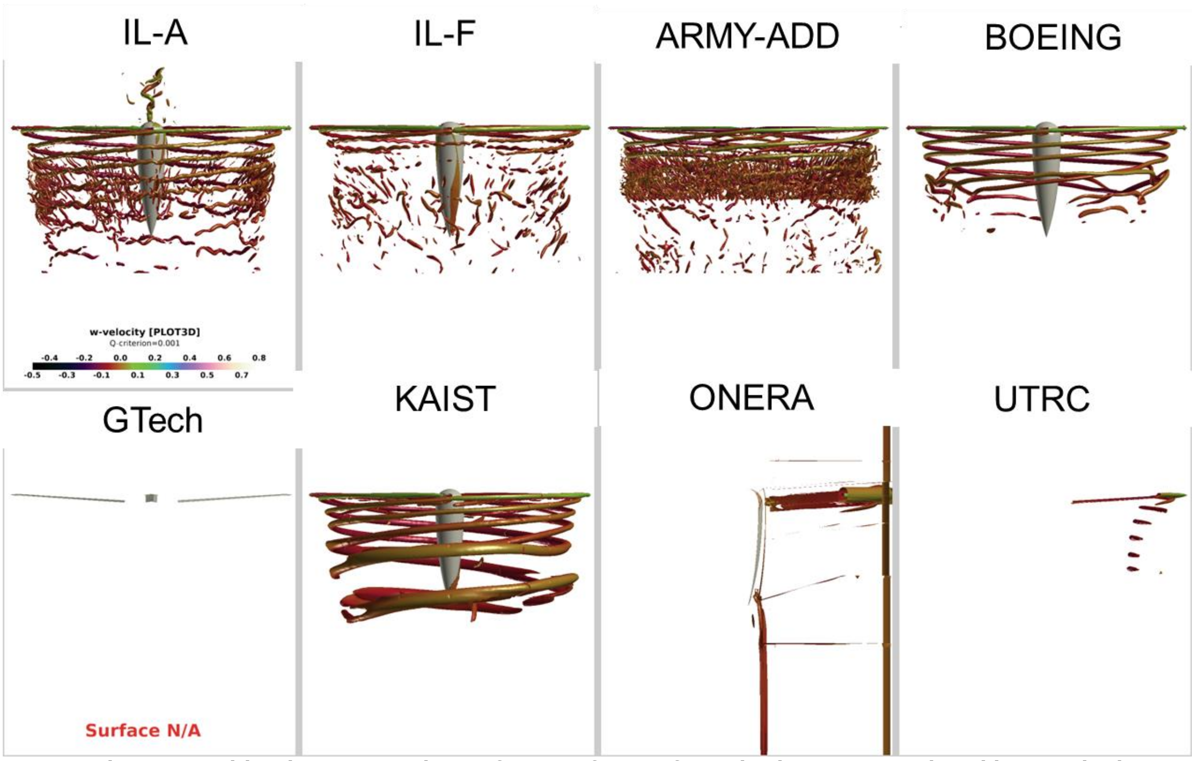

Figure 11: Side View Comparison of Iso-surfaces of Q-Criterion =0.001 colored by w-velocity

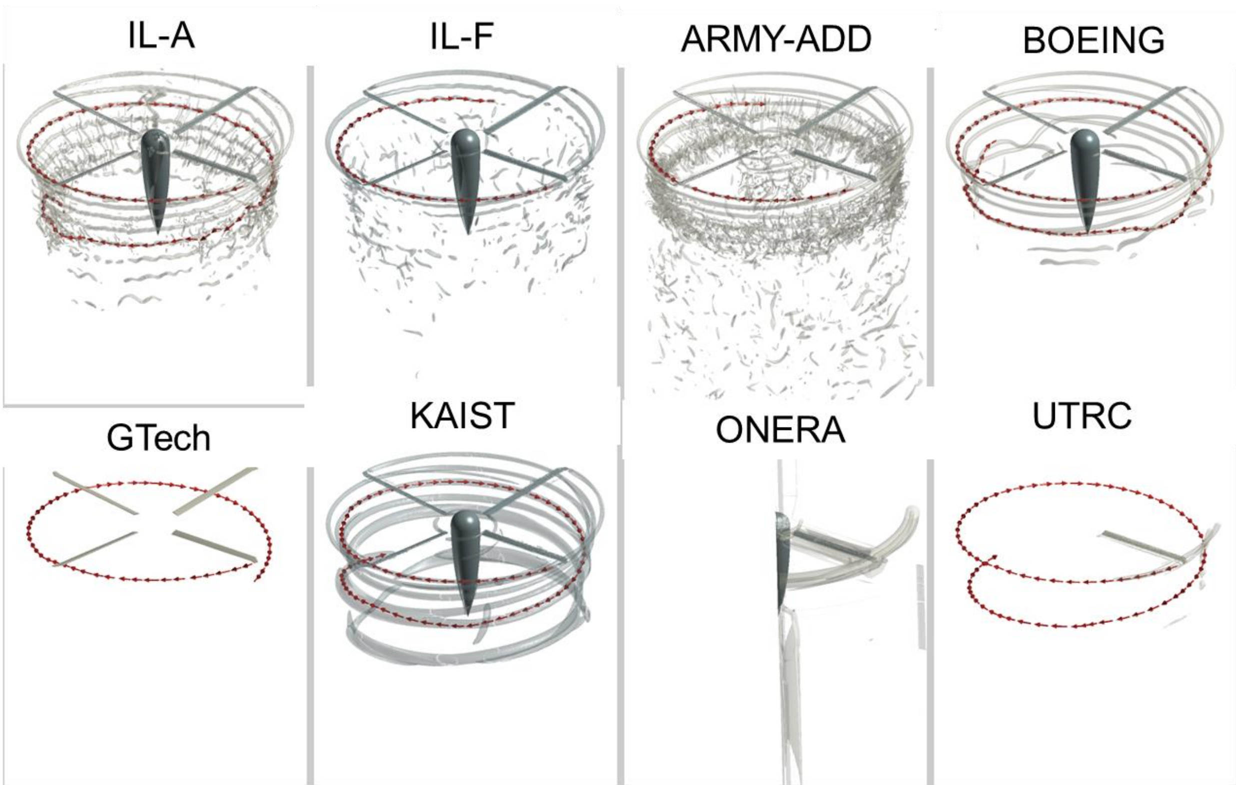

Figure 12: Q = 0.001 & Vortex Pathline

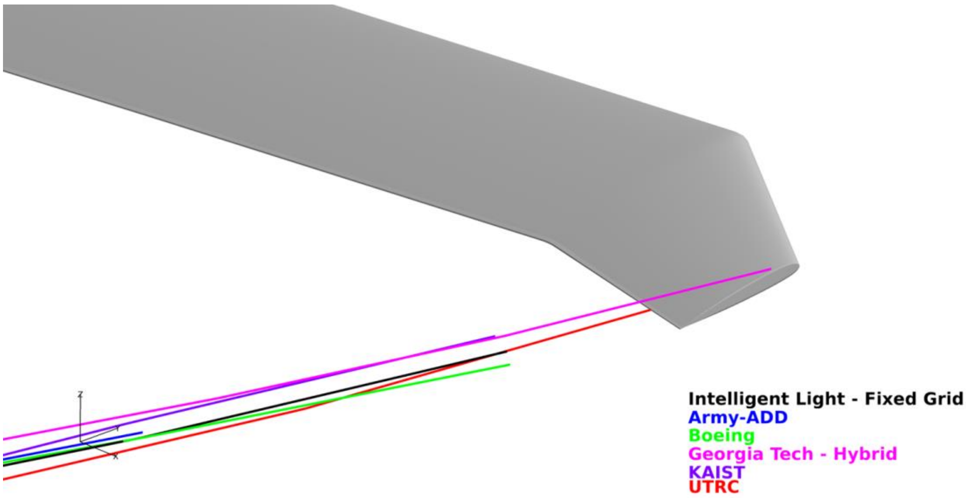

Figure 13: Vortex Core Tip Comparison

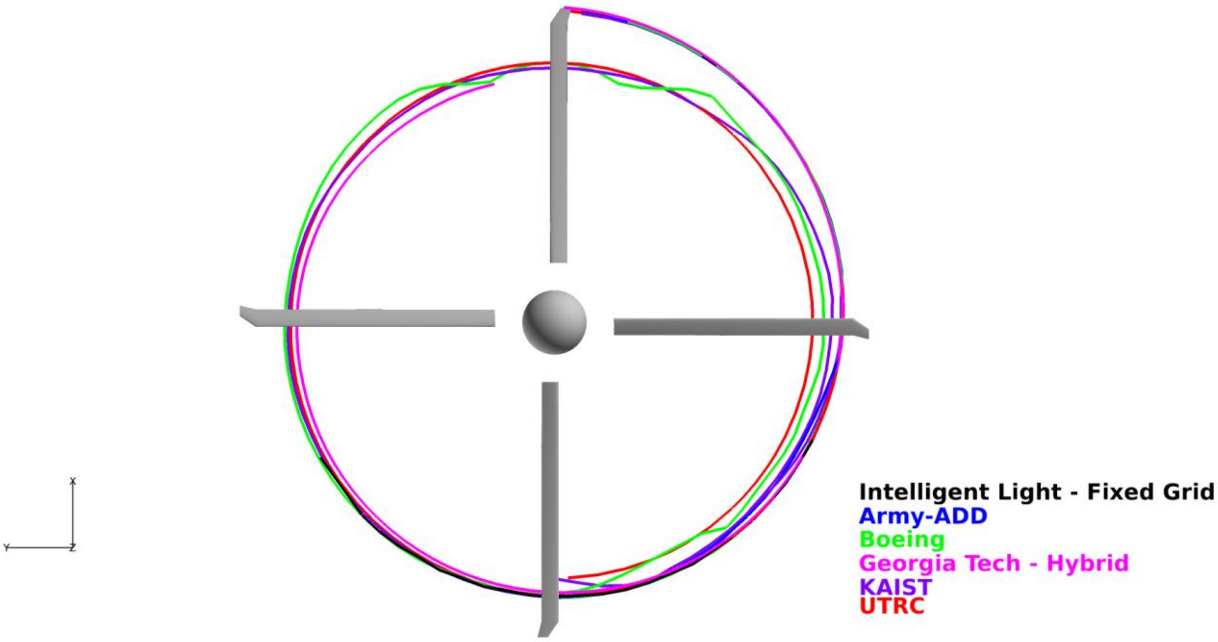

Figure 14: Vortex Core Comparing Wake Contraction

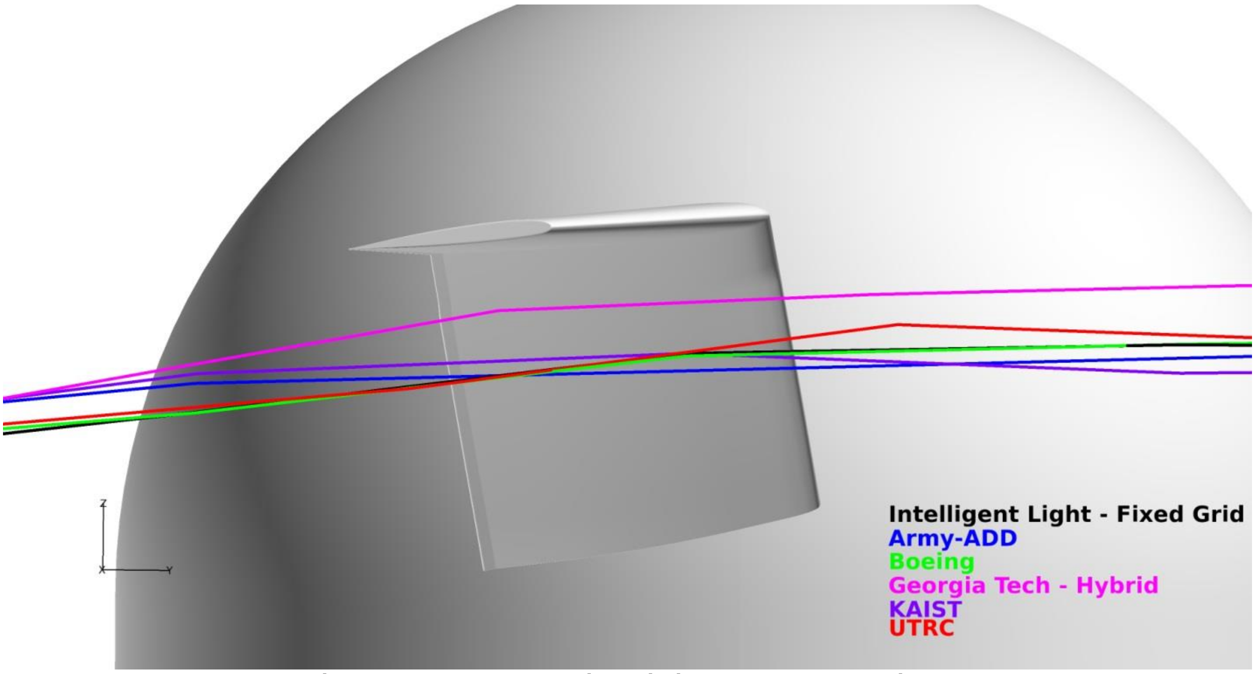

Figure 15: Vortex Core First Blade Passage Comparison

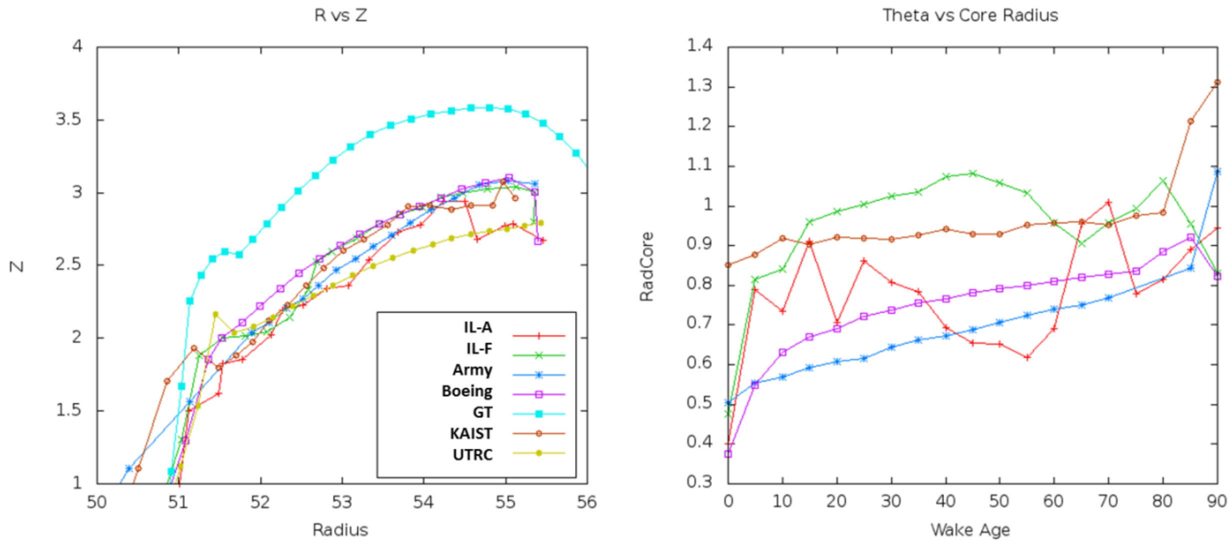

Figure 16: Wake Descent and Vortex Core Wake Age

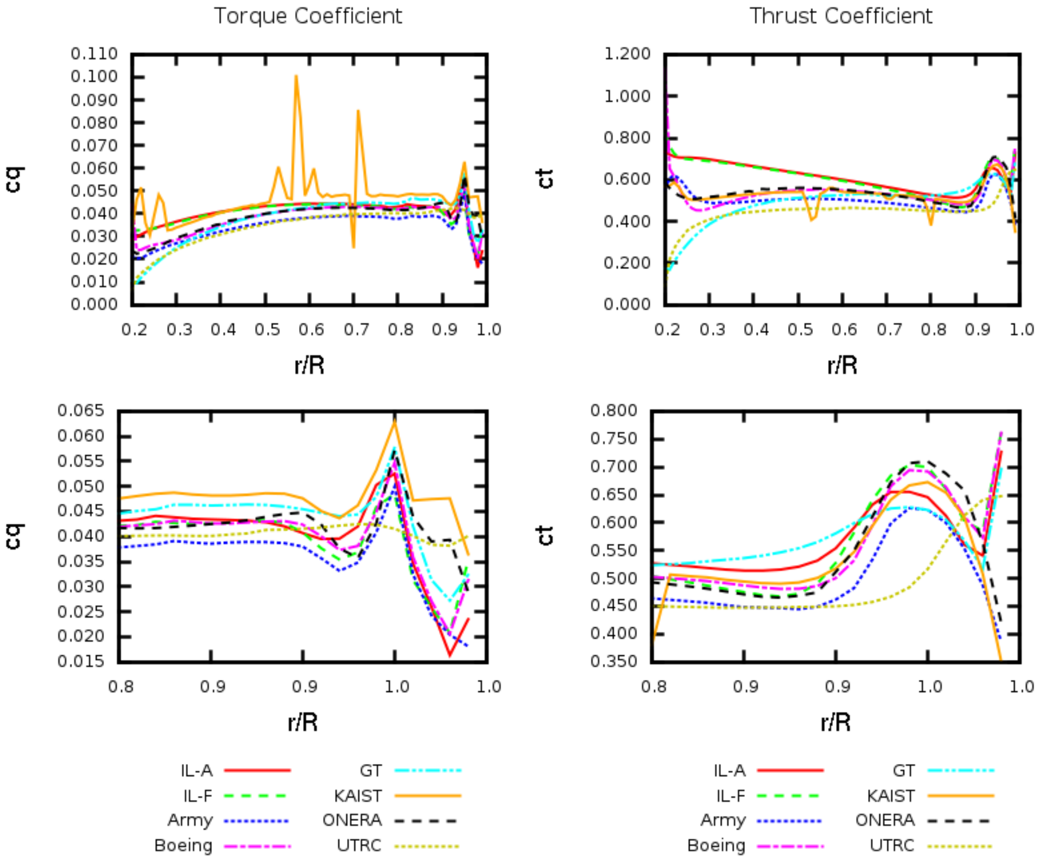

Figure 17: Torque and Thrust Coefficient Comparison

6. REFERENCES

[1] N. Hariharan, T. A. Egolf, R. Narducci and L. Sankar, "Helicopter Rotor Aerodynamic Modeling in Hover: AIAA Standardized Hover Evaluations," in *53RD AIAA AEROSPACE SCIENCES MEETING*, 2015.

[2] D. T. Balch, "Experimental study of main rotor tip geometry and tail rotor interactions in hover. Volume 1. Text and figures, NASA-CR-177336-VOL-1, NAS 1.26:177336-VOL-1," United States, Feb 01, 1985.

[3] E. Duque, M. Toyoda, M. Burklund, N. Hariharan, R. Narducci and C. Stone, "Direct Comparison of Hover Prediction Workshop Results," in *AIAA-2016-0034, 54th Aerospace Sciences Meeting and Exposition*, San Diego, CA, January 2016.

[4] R. Jain, "A Comparison of CFD Hover Predictions for the Sikorsky S-76 Rotor," in *54th Aerospace Sciences Meeting and Exposition*, San Diego, CA, AIAA-2016-0032, January 2016.

[5] H. N., R. Narducci, T. Egolf and E. Reed, "Helicopter Rotor Aerodynamic Modeling of S-76 Rotor with Tip-Shape Variations," in *AIAA-2016-0032, 54th Aerospace Sciences Meeting and Exposition*, Diego, CA, January 2016.

[6] K. Jacobson, A. Grubb and M. Smith, "Performance and Physics of a S-76 Rotor in Hover with Non-Contiguous Hybrid Methodologies," in *54th Aerospace Sciences Meeting and Exposition*, San Diego, CA, AIAA-2016-0302, January 2016.

[7] J. Hwang, J. Choi and O. Kwon, "Assessment of S-76 Rotor Hover Performance in Ground Effect Using an Unstructured Mixed Mesh Method," in *54th Aerospace Sciences Meeting and Exposition*, January 2016, AIAA-2016-0033, January 2016.

[8] P. Gardarein and A. Le Pape, "Numerical Simulation of Hover S-76 Helicopter Rotor Including Far-Field Analysis," in *54th Aerospace Sciences Meeting and Exposition*, San Diego, CA, AIAA-2016-0034, January 2016.

[9] B. Min and B. Wake, "Parametric Validation Study for a Hovering Rotor Using UT-GENCAS," in *54th Aerospace Sciences Meeting and Exposition*, January 2016, AIAA-2016-0301, January 2016.